Journal of Biomedical Optics

BiomedicalOptics.SPIEDigitalLibrary.org

Determination of the radiance of cylindrical light diffusers: design of a one-axis charge-coupled device camera-based goniometer setup

Andreas Pitzschke
Jenny Bertholet
Blaise Lovisa
Matthieu Zellweger
Georges Wagnières

SPIE.

Andreas Pitzschke, Jenny Bertholet, Blaise Lovisa, Matthieu Zellweger, Georges Wagnières, "Determination of the radiance of cylindrical light diffusers: design of a one-axis charge-coupled device camera-based goniometer setup," *J. Biomed. Opt.* **22**(3), 035004 (2017), doi: 10.1117/1.JBO.22.3.035004.

Determination of the radiance of cylindrical light diffusers: design of a one-axis charge-coupled device camera-based goniometer setup

Andreas Pitzschke, Jenny Bertholet, Blaise Lovisa, Matthieu Zellweger, and Georges Wagnières*
Swiss Federal Institute of Technology (EPFL), Institute of Chemical Sciences and Engineering, Lausanne, Switzerland

Abstract. A one-axis charge-coupled device camera-based goniometer setup was developed to measure the three-dimensional radiance profile (longitudinal, azimuthal, and polar) of cylindrical light diffusers in air and water. An algorithm was programmed to project the two-dimensional camera data onto the diffuser coordinates. The optical system was designed to achieve a spatial resolution on the diffuser surface in the submillimeter range. The detection threshold of the detector was well below the values of measured radiance. The radiance profiles of an exemplary cylindrical diffuser measured in air showed local deviations in radiance below 10% for wavelengths at 635 and 671 nm. At 808 nm, deviations in radiance became larger, up to 45%, most probable due to the manufacturing process of the diffuser. Radiance profiles measured in water were less Lambertian than in air due to the refractive index matching privileging the radial decoupling of photons from the optical fiber. [DOI: 10.1117/1.JBO.22.3.035004]

Keywords: radiance; cylindrical light diffuser; photodynamic therapy; emission profile; optical radiation measurement; video camera; imaging.

Paper 160782RR received Nov. 21, 2016; accepted for publication Feb. 16, 2017; published online Mar. 10, 2017.

1 Introduction

Cylindrical light diffusers are devices used for the administration of light doses in clinical procedures, such as photodynamic therapy (PDT) and interstitial laser photocoagulation (ILP). They combine the efficiency and flexibility of an optical fiber with a compact light delivery system that can easily be inserted in a catheter, a cannula, or the biopsy channel of an endoscope. Cylindrical light diffusers are used in particular during PDT to illuminate hollow organs, such as the bronchus, trachea, esophagus, coronary arteries or endometrium,[1–4] or interstitially in the prostate.[5] These devices are also used to increase the volume of necrosis induced by ILP[6,7] and in nonclinical fields, e.g., in light dosimetry[8] and for the measurement of tissue optical properties.[9]

A primary concern of these applications is the accuracy and precision to deliver the light dose to the target tissue. Significant variations in the irradiance can lead to localized hot and cold spots resulting in undesirable irradiation effects. The usage of "long" wavelengths, above 700 nm, to excite photosensitizers, such as those developed for prostate cancer and bronchial PDT,[10–12] further enhances the impact of a heterogeneous illumination, e.g., unanticipated necrosis geometries, due to the increased penetration depth. Paradoxically, manufacturers often supply only a radial light emission measurement as proof of quality. The measurement of the light distribution along the length of the diffuser can be constant and may give the impression that the diffuser has a good performance. However, this procedure fails to measure in other directions that may have a different distribution and magnitude of emitted power. The radiance, which is the key directional radiometric parameter, is rarely given in the specifications. This situation is usually unproblematic for the interstitial usage of these diffusers. The light distribution becomes isotropic in the tissue at a depth of a few $\mu_s'^{-1}$ from the diffuser's surface, where μ_s' is the reduced scattering coefficient and in the order of 1 mm^{-1} for most soft tissues between 630 and 950 nm.[13] However, the picture is quite different when the light diffuser is inserted in a large hollow organ. In such a situation, a forward-peaked emission of the light may result in a "translation" of the illumination spot relative to the light diffuser, as described by Farina et al.[14] Even when accurate specifications are supplied by the manufacturer, they can sometimes be of limited use as they are based on measurements performed in air. When the diffuser is surrounded by a media with a different refractive index than that of air, e.g., soft tissue, light decoupling will differ from these specifications.[15]

Several techniques were reported for measuring more accurately the light distribution of cylindrical diffusers. Common methods involve simple photographs taken from the emitting diffuser,[16] measurements of longitudinal and circumferential profiles with cleaved fibers,[17] isotropic probes,[14,17–19] detectors with pinholes,[20–24] or integrating spheres.[14,25] Murrer et al.[26] proposed a setup where a head mounted with five detectors at different angles (30 deg, 60 deg, 90 deg, 120 deg, and 150 deg) is measuring the longitudinal and azimuthal radiance profile. By rotating the diffuser, also the polar radiance profile can be measured, which eventually permits a full three-dimensional description of the diffuser radiance profile. This setup is, however, limited to a low spatial resolution in the azimuthal direction. In general, the setups to determine the circumferential profiles consist either of a stationary detector or charge-coupled device (CCD) camera measuring the polar profile of a rotating

*Address all correspondence to: Georges Wagnières, E-mail: georges.wagnieres@epfl.ch

1083-3668/2017/$25.00 © 2017 SPIE

fiber,[20,24,26,27] or of a goniometer setup, where the diffuser is fixed in the rotation center of the movable detector system,[21–23,28] which measures the polar and/or azimuthal profile.

Most of the techniques measure the absolute or normalized light intensity, irradiance, or emittance in air, which are all of limited use when Monte-Carlo methods are employed to simulate the light propagation in organs.[8,14] In that case, the radiance profile of the diffuser is needed to correctly compute the fluence distribution in tissue. Measurements of the fluence rate in Intralipid/Lipovenös solutions (6% to 20%)[14,25,26,28] or fluorescence dyes[16,29] are suited for interstitial applications, but are of limited use for treatments of hollow organs. Especially fluorescence imaging techniques have drawbacks related to the availability of suitable fluorescence dyes and the appropriate filters for the wavelength of interest. Intralipid or Lipovenös solutions simulate the light scattering of the tissue in the vicinity of the diffuser, yet a single lipid concentration is only usable for the specific scattering coefficient of the solution. To our knowledge, there is no general approach to measure the three-dimensional radiance profile of a cylindrical diffuser in a solution with a refractive index close to that of tissue, which can eventually be used as input for a Monte-Carlo model.

The main objective of this project was to propose a setup of a one-axis goniometer to measure the radiance at the surface of cylindrical light diffusers. This setup, which is based on the use of a CCD camera, allows characterization of the three-dimensional radiance with help of an in-house developed image-data processing software. The measurement can be performed in air or a liquid with a specific refractive index. The setup is absolutely calibrated with the help of an integrating sphere. We also fully characterized a commercially available and exemplary type of cylindrical diffuser as validation of our setup.

2 Materials and Methods

2.1 *Radiometric Definitions*

For the sake of clarity, some definitions of radiometric quantities are summarized in the following. A more general overview on radiometry can be found in text books.[30]

The irradiance E (Wm^{-2}) is the radiant flux (power) received by a surface per unit area. The power radiated by the surface of a body per unit area is called emittance M (Wm^{-2}) and has the same unit as the irradiance. The defining equation is $M = \mathrm{d}\Phi/\mathrm{d}A$, where $\mathrm{d}\Phi$ is an element of radiant flux and $\mathrm{d}A$ is an element of an area. Irradiance and emittance are functions of position on the specified surface. Thus, they are important quantities when describing radiation incident or leaving a surface when it is not essential to describe the angular or directional distribution of this radiation in detail. The radiant intensity I (Wsr^{-1}) is the radiant flux per unit solid angle incident on, passing through, or emerging from a surface and propagating in a specified direction. The defining equation is $I = \mathrm{d}\Phi/\mathrm{d}\Omega$. The radiant intensity is usually a function of the direction. The radiance L ($\mathrm{Wm}^{-2}\ \mathrm{sr}^{-1}$) is the radiant flux per unit projected area and per unit solid angle incident on, passing through, or emerging in a specified direction from a specified point in a specified surface. The defining equation is

$$L = \frac{\mathrm{d}^2\Phi}{\mathrm{d}A\,\mathrm{d}\Omega} = \frac{\mathrm{d}^2\Phi}{\mathrm{d}A_0\,\mathrm{d}\Omega\,\cos\theta}, \tag{1}$$

where $\mathrm{d}A = \mathrm{d}A_0\,\cos\theta$ is called the projected area, i.e., the area of the projection of an elemental area $\mathrm{d}A$ in the plane containing the point at which the radiance is being defined and that is perpendicular to the direction specified by L. $\mathrm{d}\Omega$ is an element of solid angle in this direction and θ is the angle between this direction and the normal to the surface at the specified point. The radiance is a function of the position and the direction of the emitted light ray; therefore, it is the most general quantity for describing the propagation of radiation.

For a Lambertian surface, the intensity I_θ at a point on a surface varies with direction. It is proportional to the cosine of the angle defined between the viewing direction and the normal to the emitting surface ($I_\theta = I_0\,\cos\theta$). Unlike intensity, the radiance is constant for different values of θ, since the term "cos θ" is canceled by the same term appearing in the definition of the projected area $\mathrm{d}A$.

2.2 *Experimental Setup*

2.2.1 *Goniometer setup*

The developed one-axis CCD camera-based goniometer setup enables the measurement of the radiance of a light source located in the goniometer rotation center. The radiance can be measured in all dimensions (longitudinal, azimuthal, and polar) and in air or liquid. The measurements reported here were performed by recording images of a cylindrical light diffuser. The light diffuser was positioned, parallel, or perpendicular to the axis in the center of a rotating platform, on which a mechanical arm holding a CCD camera was fixed (Fig. 1). Each image was mapped onto the two-dimensional geometry of the diffuser surface. Cylindrical coordinates ($\rho = \mathrm{const.}, \phi, z$) were used to represent a position on the diffuser.

Positioning the diffuser horizontally allowed the measurement of the radiance as function of the azimuthal angle θ [Fig. 2(a)], (x, z)-plane, for a range in poloidal angle of ϕ from -60 deg to 60 deg. An image $(x_{\mathrm{CCD}}, y_{\mathrm{CCD}})$ taken by the detector array at a given angle θ allowed for the reconstruction of the radiance as function of z and ϕ with the coordinate transformation $x_{\mathrm{CCD}} \rightarrow z$ and $y_{\mathrm{CCD}} \rightarrow \phi$. It was assumed that the radiance was symmetric in ϕ [Fig. 2(b)], so that measurements at different y_{CCD} could be attributed to a single surface element. It is important to note that an azimuthal angle θ close to 0 deg and 180 deg was inaccessible to the line of sight of the camera

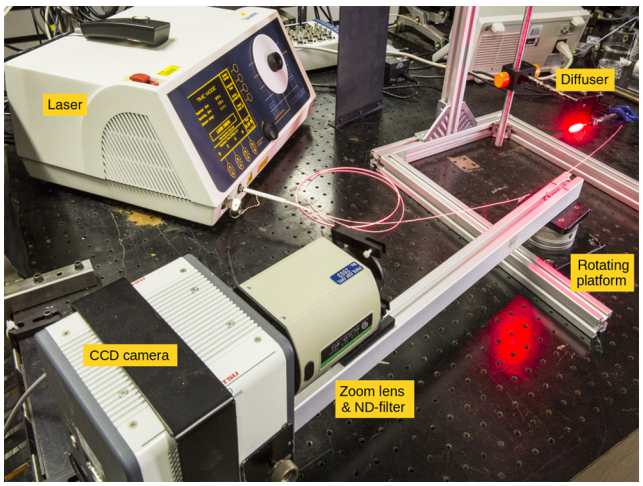

Fig. 1 Goniometer setup: rotating platform, mechanical arm with CDD camera, neutral density filter, and diffuser holder.

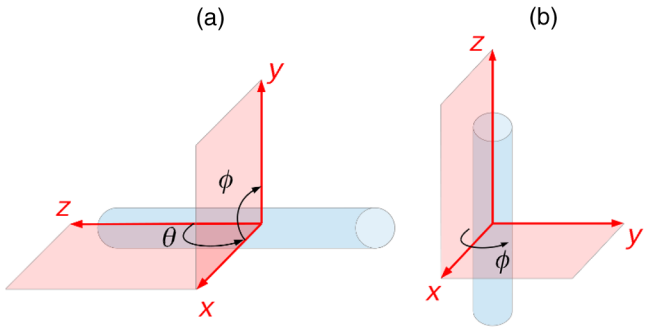

Fig. 2 Diffuser alignment: (a) horizontally allowing for the measurement of $L(\theta,\phi,z)$ and (b) vertically for the measurement of $L(\phi,z)$. The CCD detector x_{CCD}, y_{CCD} (column, row) images the coordinates (ϕ,z) of the diffuser surface in configuration (a) and (z,ϕ) in (b).

due to the diffuser fixation blocking off the view. The loss of spatial resolution close to these angles is important, such that the absolute position of a surface element becomes inaccurate. The measurements were hence restricted to angles of θ from 30 to 150 and from 210 deg to 330 deg. For the same reason, the spatial resolution was also strongly reduced at large polar angles, i.e., $\phi > 60$ deg When fixing the diffuser vertically, the camera turned around the rotation axis of the diffuser, ϕ [Fig. 2(b)]. This configuration allowed for the measurement of the radiance as function of ϕ between ~5 deg and 355 deg and z with the coordinate transformation of $x_{CCD} \rightarrow \phi$ and $y_{CCD} \rightarrow z$ while θ was fixed to 90 deg. This configuration was used to verify our assumption of radiance symmetry in ϕ.

For the radiance measurements in water, a glass container with a light absorbing black-out coating was placed on a rotating platform in the middle of the goniometer setup (Fig. 1). The coating was necessary to avoid multiple reflections on the container wall. The container was filled with distilled water and the diffuser was submerged. The radiance measurements were carried out through a fraction of the glass container that was left out from the coating. Since the recipient was rotating together with the camera, always the same fraction of the container glass was imaged, regardless of the azimuthal angle.

2.2.2 *Light source*

One exemplary light diffuser (RD40, Medlight SA, Ecublens, Switzerland) of 40-mm length and with an outer diameter of the diffusive region of 0.98 mm was tested to validate the functionality of our setup. The fiber has a flexible plastic core of 500-μm diameter with a teflon cladding, an NA of 0.48, and an overall length of 2.5 m from the SMA 905 connector to the diffusive tip. The manufacturer indicates a fiber transmission of 70%/85%/75% at 630/652/690 nm.[31] The diffuser was connected to the laser diodes emitting at 635 nm (Ceralas PDT, 635/4W/400 μm, CeramOptec GmbH, Bonn, Germany), 671 nm (RLTMRL-671-1W, Roithner Lasertechnik GmbH, Vienna, Austria), and 808 nm (RLTMDL-808-5W, Roithner Lasertechnik GmbH, Vienna, Austria). The variation in the power output of each laser diodes was indicated by the manufacturers to be smaller than 10%. The power output of each laser was calibrated by a frontal light diffuser (FD1, Medlight SA, Ecublens, Switzerland) illuminating a power-meter (detector 818P-010-12, driver 1918-R, Spectra-Physics Newport Corp., Irvine, California) before and after the measurements. The frontal light diffuser FD1 produces a circular spot light with a uniformity of $\pm 15\%$.[32] The aperture angle of the FD1 is 34.7 deg, the fiber transmission >85%, the fiber overall diameter 2 mm, and the fiber length 4 m. The laser power was adjusted such that the output of the FD1 was ~80 to 120 mW, mainly to avoid overheating of the SMA connector during long-term use. The power output of each cylindrical diffuser (RD40) was determined by an integrating sphere with Spectraflect coating (20 in., Labsphere, North Sutton, New Hampshire) and a nonfiltered silicon detector assembly (SC-5500, Labsphere, North Sutton, New Hampshire). The integrating sphere was cross calibrated to the power-meter with the help of the FD1.

2.2.3 *CCD camera and optics*

The optical imaging system was composed of an EM-CCD camera (Hamamatsu C9100-12, Hamamatsu, Bridgewater, New Jersey), a zoom lens (Fujinon TV zoom lens H6 × 12.5R MD3, Fujinon Corporation, Saitama City, Saitama, Japan), a 1.5× C-mount extender with fixed focal point (Edmund Optics, Barrington, New Jersey), a 5-mm brass spacer ring (Edmund Optics, Barrington, New Jersey), and a neutral density transmission filter of $T = 0.1\%$ (3.0 OD 50 mm Dia, absorptive ND filter, Edmund Optics, Barrington, New Jersey) in order to suppress parasite light from reflection. The spacer ring was added to reduce the minimum working distance of the zoom lens from 1 to 0.7 m. The standard distance between camera detector and diffuser center was 0.725 m. The transmission filter was chosen such that the camera did not saturate at exposure times of 50 ms or below. The camera has a detector array of 512×512 pixels with a pixel size of 16×16 μm^2.

Prior to experiments, absolute calibration of the optical system, i.e., including the camera, the zoom lens, and the ND filter, was performed yielding a value of radiance as function of gray value. For this purpose, a diffuse reflectance standard (SRS99020, Labsphere Spectralon, North Sutton, New Hampshire) with a reflectance of >99% was irradiated by an FD1 at an angle of θ_i between 10 deg and 20 deg with respect to the Spectralon surface normal and camera viewing line. The irradiation angle was chosen to be nonzero to avoid specular reflections. This choice lead to an underestimation of the Spectralon emittance of ~2% at 635 nm. The irradiance of the Spectralon, typically $E = 1 - 20$ mW/cm^2, was calculated by $E = P/(\pi r^2)$, where P is the beam power (100 mW), d is the distance between FD1 and Spectralon (35 cm), α is the full aperture angle of the FD1 (34.7 deg), and $r = d\ \tan(\alpha/2)$ the beam radius of the FD1 spot (10.9 cm) at the Spectralon distance. The emittance and radiance were computed by $M = RE$ and $L = M/\pi$, where $R = 99\%$ is the Spectralon reflectance. Imaging the Spectralon with a known radiance yields the direct relation between radiance and gray values. The radiance of the Spectralon was found to be weakly depending on $|\theta_i - \theta_r|$, where θ_r is the angle between the Spectralon normal and the viewing direction of the camera ($-2.2\%/-4.4\%/-6.3\%$ at $|\theta_i - \theta_r| = 15/30/45$ deg). The total radiant flux of the diffuser was measured by the integrating sphere before and after the radiance measurements. This allowed for a cross verification of the absolute system calibration with the measured radiance integrated over all diffuser surface elements dA and angles dω

$$\Phi = \int_{A_0} \int_{\Omega} L \cos\theta \mathrm{d}\omega \, \mathrm{d}A. \quad (2)$$

2.2.4 *Data analysis*

The image processing software was programmed in MATLAB (R2013a, The MathWorks Inc., Natick, Massachusetts) containing modules to (1) average a stack of several images, (2) analyze the pixel noise, (3) subtract the pixel background using a background noise image, (4) remove the pixel crosstalk by signal deconvolution, (5) segment the diffuser on the image using a Canny edge detection algorithm (MATLAB and Image Processing Toolbox R2013a), (6) map the two-dimensional gray values on the corresponding diffuser geometry, (7) visualize intensity and radiance as function of (z, θ, ϕ), and (8) compute the total radiant flux.

3 Results

3.1 *System Performances*

3.1.1 *Spatial resolution of the goniometer setup*

The total magnification of the optical system was determined by imaging a reference grid pattern (1951 USAF Hi-Resolution target, Edmund Scientific, North Sutton, New Hampshire). The typical spatial resolution of the longitudinal coordinate was $\Delta z \approx 100 - 140$ μm for an azimuthal and polar angles of $\theta = 90$ deg and $\phi = 0$ deg. The spatial resolution at the diffuser surface is given by $\Delta z(\theta) = \Delta z(\theta = 0)/\sin\theta$ and $\Delta\phi(\phi) = \Delta\phi(\phi = 0)/\cos\phi$, such that typical values of $\Delta z \approx 175 - 245$ μm for $\theta = 30$ deg and $\Delta z \approx 385 - 540$ μm for $\phi = 75$ deg could be achieved.

3.1.2 *Linearity of the imaging system*

The linear response of the camera was verified by imaging a graded linear filter (EIA linear gray scale 20:1, Edmund Scientific, North Sutton, New Hampshire) illuminated by a white light source. The camera response was found to be approximately linear for an incident radiant flux Φ above 50% of the cameras dynamic range [Fig. 3(a)]. Therefore, experiments were carried out within $50\% - 60\%$ of the dynamic range with a relative signal uncertainty of $u(S)/S \leq 2\%$ $(k = 1)$.

3.1.3 *Pixel crosstalk of the CCD camera detector*

The pixel crosstalk of the CCD camera detector was investigated in the range of $5\% - 90\%$ of the maximal detector count. A pinhole with a diameter of 0.1 mm was homogeneously back-illuminated by an FD1 at 635 nm and imaged by the camera at a distance of 5 m, such that the pinhole was projected on a single pixel in the center of the detector. The image background, an average of a stack of 10 images taken before illumination of the pinhole, was subtracted from the individual images taken at different light intensities.

The signal of the pixels in the vicinity of the illuminated pixel was found to be proportional to the imaged pinhole intensity. The pixel response at different signal levels showed the same blooming behavior, such that all response profiles were normalized to their maximum value and then averaged. The averaged response profiles for the pixel rows (x_{CCD}) and columns (y_{CCD}) are shown in Figs. 3(b) and 3(c), together with the standard deviation ($k = 2$). The overall pixel crosstalk was found to be less than 5%. Close to the illuminated pixel, the pixels in the same row showed a higher cross talk, up to 60%, which may be due to the charge shifting in the pixel row during the detector readout. The maximal standard deviation of the averaging procedure was 9% ($k = 1$). The point spread functions were used as input for the deconvolution of the data as function of x_{CCD} and y_{CCD}.

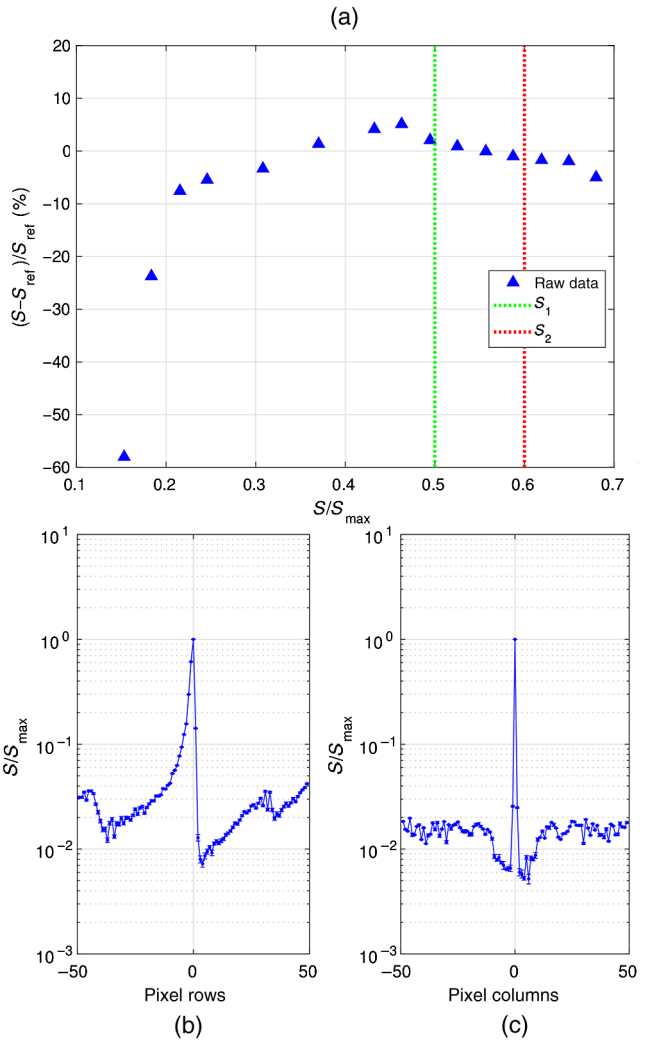

Fig. 3 (a) Deviation of the camera signal S with respect to the ideal linear response S_{ref}. S_1 and S_2 denote the signal range used for radiometric measurements. (b) and (c) Normalized pixel signal (rows and columns), when imaging a pinhole.

3.1.4 *Detection limit of the imaging system*

The radiance is given by

$$L = f_c f_d f_l (S - S_0), \quad (3)$$

where S (gray value, gv) is the detector signal, S_0 (gv) is the detector background signal, f_c (mW cm^{-2} sr^{-1} gv^{-1}) is the calibration factor, f_d is the correction factor from the signal deconvolution, and f_l is the correction factor from the signal linearity.

The characteristic limits of the imaging system were computed according to ISO 11929:2010. The ISO standard defines the decision threshold L^* and detection limit $L^\#$ as follows:

$$L^* = k_p u(0), \tag{4}$$

$$L^{\#} = L^* + k_q u(L^{\#}), \tag{5}$$

where k_p and k_q are the quantiles of the standard normal distribution for the probabilities $p = 1 - \alpha$ and $q = 1 - \beta$. The probability of the error of the first and second kinds in Eqs. (4) and (5) was set to $\alpha = \beta = 5\%$, such that $k_p = k_q = 1.65$. The physical effect is assumed to be absent below the decision threshold. For values between decision threshold and detection limit, the effect is assumed to be present, but not quantifiable. Above the detection threshold, the physical effect is quantifiable. By substituting the correction factors with $w = f_c f_d f_l$, the uncertainty of the radiance $u(L)$ is given by

$$u(L) = \sqrt{w^2[u^2(S) + u^2(S_0)] + L^2 u_{\mathrm{rel}}^2(w)}, \tag{6}$$

$$u_{\mathrm{rel}}^2(w) = \left[\frac{u(f_c)}{f_c}\right]^2 + \left[\frac{u(f_d)}{f_d}\right]^2 + \left[\frac{u(f_l)}{f_l}\right]^2. \tag{7}$$

Typical values and their relative standard uncertainties ($k = 1$) used for the computation of the decision threshold and the detection limit can be found in Table 1. The relative uncertainty in the radiance $u(L)/L$ is derived from Eq. (6), $u(S)/S$ and $u(S_0)/S_0$ correspond to the standard deviation of the signal normal distribution normalized by the detector signal in the presence and the absence of an illuminating light, $u(f_c)/f_c$ is the standard deviation of the calibration factors from $\sim 100 \times 100$ pixels normalized by their mean value, $u(f_d)/f_d$ is the maximum standard deviation of the point-spread-function of the detector pixels within the range of 0.2 to 0.9 of the maximum detector signal (16,384 counts) [Figs. 3(b) and 3(c)], and $u(f_l)/f_l$ is the maximum deviation of the detector signal from the ideal response within the range of signal used for the measurements [Fig. 3(a)].

The decision threshold was found to be $L^* = 15\ \mu\mathrm{W\,cm^{-2}\,sr^{-1}}$. By solving Eq. (5) iteratively, a detection limit of $L^{\#} = 75\ \mu\mathrm{W\,cm^{-2}\,sr^{-1}}$ was computed. The detection limit compared with a signal-to-noise ratio of $S/N \approx 8$. The relatively high detection threshold is due to the nonlinearity of the camera as presented in Fig. 3(a). By suppressing the ND filter, the detection threshold may decrease, yet parasite light will become more prominent. The measured values of radiance, presented in the following, were always well above the detection limit (by a factor of 10 or more).

Table 1 Characteristic quantities of the imaging system and their relative uncertainties.

Quantity	Symbol	Value	Relative std. uncertainty (%)
Radiance	L	3.46 $\mathrm{mW\,cm^{-2}\,sr^{-1}}$	3.1
Detector signal	S	9000 gv	2.2
Detector background signal	S_0	504 gv	1.5
Calibration factor	f_c	0.41 $\mu\mathrm{W\,cm^{-2}\,sr^{-1}\,gv^{-1}}$	1.1
Signal deconvolution	f_d	0 to 1	9.0
Linearity correction	f_l	1	2.0

3.2 *Radiometric Measurements*

3.2.1 *Measurements at different wavelengths*

In the following, data of an exemplary RD40 diffuser are shown. Figure 4 shows an example of the normalized radiance of the RD40 measured in air. Measurements were carried out at wavelengths of 635, 671, and 808 nm. Points represent individual detector pixels with a spatial resolution of $(\Delta z, \Delta\theta, \Delta\phi) = (124\ \mu\mathrm{m}, 15\ \mathrm{deg}, 13\ \mathrm{deg})$. Lines represent the spline interpolation of the experimental data on a grid with a resolution of $(\Delta z, \Delta\theta, \Delta\phi)_{\mathrm{spline}} = (200\ \mu\mathrm{m}, 4\ \mathrm{deg}, 4\ \mathrm{deg})$. The interpolant grid was chosen to be a compromise of good spatial resolution in z at different angles θ and a sufficiently high resampling of the experimental data in θ and ϕ in order to increase the precision of the total radiant flux calculation by integrating Eq. (2) over all coordinates.

Figures 4(a)–4(c) show the normalized radiance as function of the diffuser length z and the angles θ and ϕ, respectively. Profiles in z are shown for $\theta = 90$ deg and $\phi = 0$ deg. The proximal and distal ends of the diffuser are at approximately $z = -22$ mm and $z = 22$ mm, respectively. The normalized radiance as function of θ is shown for $\phi = 0$ deg and $z = 0$ mm, i.e., at the center of the diffuser. The normalized radiance as a function of ϕ is shown for $\theta = 90$ deg and $z = 0$ mm. A general tendency was that inhomogeneities in the radiance became larger when the wavelength increased. Table 2 summarizes the standard deviation in radiance $\sigma(L)$ and the maximal variation in radiance $\delta_{\max}(L)$ as function of the individual coordinates. Both quantities were computed from the profiles defined by $-20 \le z \le 20$ mm, $30\ \mathrm{deg} \le \theta \le 150$ deg, $210\ \mathrm{deg} \le \theta \le 330$ deg, and $-60\ \mathrm{deg} \le \phi \le 60$ deg [Figs. 4(a)–4(c)]. As a simplification, data are only given for sets of (z, θ, ϕ) of major interest, i.e., $\sigma[L(z)]$ for $(\theta, \phi) = (0\ \mathrm{deg}, 0\ \mathrm{deg})$, $\sigma[L(\theta)]$ for $(z, \phi) = (0\ \mathrm{mm}, 0\ \mathrm{deg})$, and $\sigma[L(\phi)]$ for $(z, \theta) = (0\ \mathrm{mm}, 0\ \mathrm{deg})$. Identical conditions were chosen for evaluating $\delta_{\max}(L)$. The standard deviation and maximum variation in radiance were only computed for a semisphere, i.e., $\theta = [0, 180]$ deg, to avoid a systematic bias of the absolute or normalized value of radiance due to misalignment of the RD40 with respect to the goniometer center. As in Figs. 4(a)–4(c), the standard deviation of L increased with increasing wavelength and $\delta_{\max}(L)$ was observed to be largest at 808 nm. At wavelengths of 635 and 671 nm, $\sigma(L)$ was comparable, whereas $\delta_{\max}(L)$ was slightly higher at 671 compared to 635 nm.

Integrating the spline-fitted radiance over the azimuthal and polar angles as well as all surface elements yields the total radiant flux, summarized in Table 3. The relative uncertainty of the integrating sphere calibration, which was estimated by linear regression of the detector signal as function of the input power, was 1.5% ($k = 1$). The results showed that the measured and computed total radiant flux agreed well. The value obtained from integration consistently underestimated the measured flux, which may be attributed to an imperfect representation of radiance at azimuthal angles close to 0 deg and 180 deg. For the wavelength of 808 nm, it remained unclear why the total radiant flux Φ_{CCD} underestimated by up to 15% the value measured by the integrating sphere Φ_{sphere}.

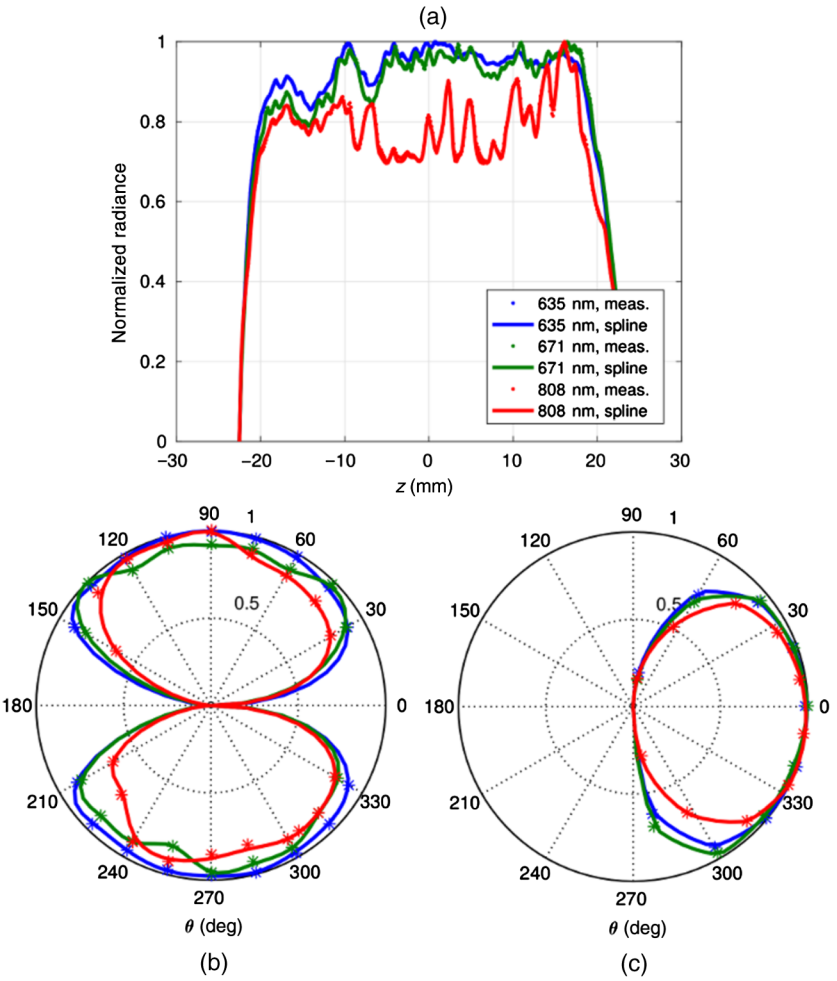

Fig. 4 Profiles of the normalized radiance as a function of (a) z ($\theta = 90$ deg, $\phi = 0$ deg), (b) θ ($z = 0$ mm, $\phi = 0$ deg), and (c) ϕ ($z = 0$ mm, $\theta = 90$ deg) for wavelengths at 635,671, and 808 nm. Dots show the raw data and the solid lines show the spline-fitted data. The proximal and distal ends of the diffuser are at $(z, \theta) = (-20$ mm, 180 deg) and (20 mm, 0 deg), respectively. The maximum radiance was 5.1/4.4/3.8 mW cm^{-2} sr^{-1} for a laser output measured by the FD1 of 100/100/380 mW at 635/671/808 nm.

3.2.2 *Measurements in water*

The radiance profile as function of the diffuser length was measured in air, in air with glass container, and in water with glass container for 635 nm (Fig. 5). Absolute values of radiance decreased by ~12% when adding the glass container (w/o water) due to the Fresnel reflections at the two glass interfaces. By adding water to the container, the radiance decreased further by ~5%. Figures 6(a)–6(c) show the normalized radiance in air with the glass container in place and in water for a wavelength of 635 nm. The radiance as a function of z in water was reduced by up to 12% at the proximal end ($z < 0$ mm) and increased by up to 6% at the distal end ($z > 0$ mm) with respect to the values obtained in air. The radiance as a function of the azimuthal and polar angles was more radially peaked. The standard deviation of the normalized radiance $\sigma(L)$ and the maximum

Table 2 Standard deviation of the normalized radiance $\sigma(L)$ and the maximum variation $\delta_{max}(L) = \min\{L\} - 1$ as function of z, θ, ϕ, and the wavelength λ.

	$\sigma(L)$			$\delta_{max}(L)$		
λ (nm)	z (%)	θ (%)	ϕ (%)	z (%)	θ (%)	ϕ (%)
635	5	5	5	−15	−10	−10
671	5	5	5	−20	−15	−10
808	10	15	10	−30	−45	−20

Table 3 The total radiant flux measured by the integrating sphere Φ_{sphere} and the integral of the radiance measured by the CCD camera-based goniometer setup Φ_{CCD} as function of the wavelength λ. Φ_{CCD} was computed with Eq. (2).

λ (nm)	Φ_{sphere} (mW)	Φ_{CCD} (mW)	Φ_{CCD}/Φ_{sphere}
635	87 ± 3	83	0.95
671	120 ± 4	112	0.93
808	117 ± 4	101	0.86

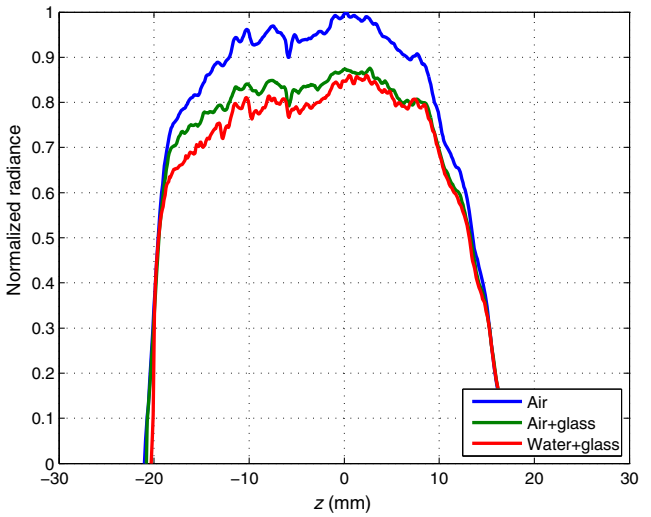

Fig. 5 Normalized radiance in air, in air with the glass container, and in water. The proximal and distal ends of the diffuser are at $z < 0$ mm and $z > 0$ mm, respectively. The maximum radiance in air was 5.1 mW cm^{-2} sr^{-1} for a laser output measured by the FD1 of 100 mW at 635 nm.

Table 4 Standard deviation of the normalized radiance $\sigma(L)$ and the maximum variation $\delta_{\max}(L) = \min\{L\} - 1$ for the two media, air and water.

	$\sigma(L)$			$\delta_{\max}(L)$		
Medium	z (%)	θ (%)	ϕ (%)	z (%)	θ (%)	ϕ (%)
Air	5	5	5	−15	−30	−20
Water	5	10	10	−35	−40	−35

variation $\delta_{\max}(L) = \min\{L\} - 1$ is summarized in Table 4 for air and water. The values were computed according to the intervals used for obtaining the data listed in Table 2.

4 Discussion

Most CCD detectors are made of silicon, which can detect electromagnetic radiation over a wavelength range of 350 to 1100 nm. This range of operation is particularly useful, because it covers the wavelengths used for PDT (630 to 675 nm) and ILP

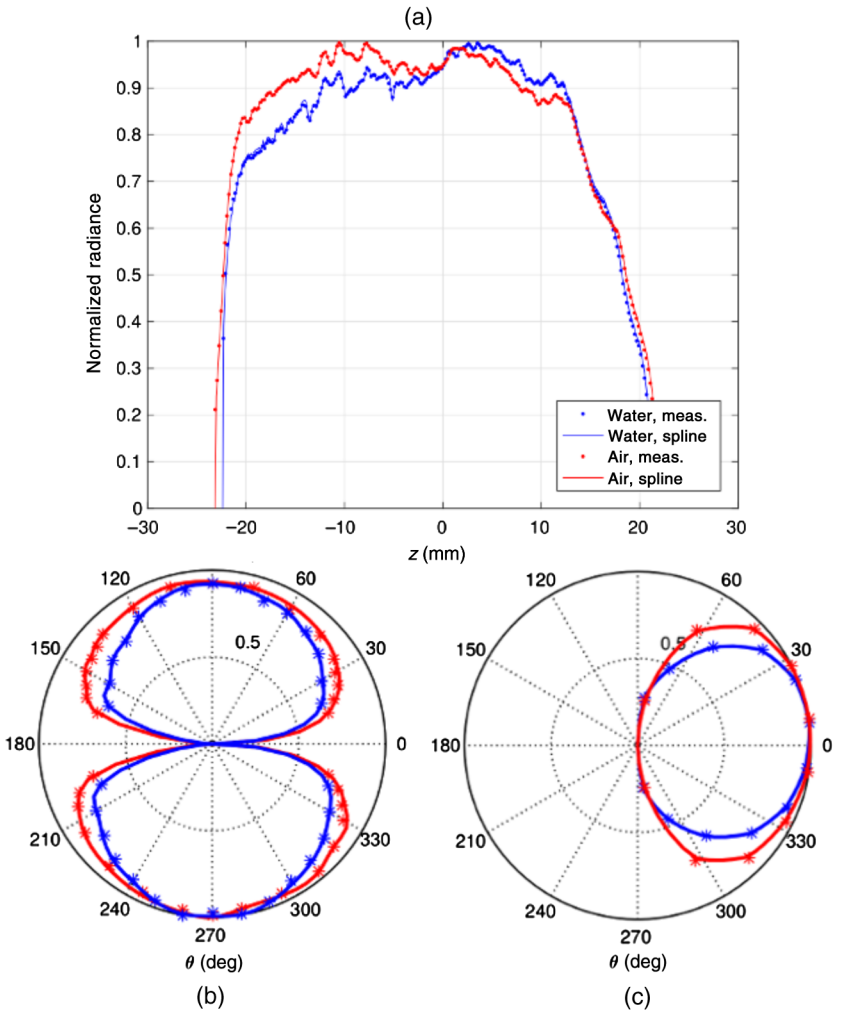

Fig. 6 Profiles of the normalized radiance as a function of (a) z, (b) θ, and (c) ϕ in air and water at 635 nm. Dots show the raw data and the solid lines show the spline-fitted data. The proximal and distal ends of the diffuser are at $(z, \theta) = (-20$ mm, 180 deg) and (20 mm, 0 deg), respectively. The maximum radiance in air and water was 5.1 and 4.4 mW cm^{-2} sr^{-1}, respectively, for a laser output measured by the FD1 of 100 mW at 635 nm.

(800 to 1064 nm). The combination of such a CCD detector with the rotational mount allows for the measurement of the radiance along the diffuser as well as all angular components by performing a single scan along the azimuthal angle. The developed data processing algorithm enable us to reconstruct a highly resolved three-dimensional distribution of the radiance with a spatial resolution in the submillimeter range. The imaging system has a high performance that can reliably detect radiance values down to 0.1 $\mathrm{mW\,cm^{-2}\,sr^{-1}}$ and most likely below when measuring without the neutral density filter. The longitudinal and angular profiles measured in air and water give an indication of the quantitative data produced by this technique. The results from the longitudinal data compare favorably with the manufacturer's data sheet.

The longitudinal profiles at the wavelengths of 635, 671, and 808 nm are very homogeneous with a standard deviation of the normalized radiance being usually below 10%. The increase in the standard deviation with increasing wavelength may be attributed to the manufacturing process of the diffuser, which is optimized for PDT applications, i.e., in the range of 630 to 690 nm.[31] Especially above 700 nm, light absorption in plastic fibers largely increases with increasing wavelength due to the excitation of higher vibrational states of the phenyl group,[33] which may result in larger profile inhomogeneities. At 808 nm, relative variations in the profile are maximal, which may become an issue depending on the application. Variations in the irradiance of the tissue, which are significantly different from the average, produce localized hot and cold spots in the light distribution. The occurrence of hot spots can lead to photobleaching[34] of the photosensitizing drug and/or hyperthermia.[1,3] These effects are undesirable and can lead to ineffective tumor cell kill and hence local recurrence of the disease. When applied in photobiomodulation,[8] inhomogeneities in tissue irradiance may trigger unpredictable cellular responses.

No pronounced forward-directed emission was detected, in contrary to what was reported for diffusers from several other independent manufacturers.[21–24,27,29] The azimuthal profile is nearly Lambertian at 635 nm, only at increasing wavelength, inhomogeneities become more prominent. Light transmission in these plastic fibers was observed to be significantly lower in the NIR than in the visible range, by a factor of 3 to 4, when compared to the silica fiber of the frontal diffuser FD1. Although the exact fiber composition of the RD40 is unknown, this result is in accordance with the higher light attenuation of plastic fibers in the NIR.[33]

The measured azimuthal and polar radiance profiles of the RD40 in water are less Lambertian. This effect can be attributed to the change in the refractive index when measuring in air or water. Snell's law predicts a more isotropic emission of light when the refractive index outside the diffuser increases (from $n_{\mathrm{air}} = 1$ to $n_{\mathrm{water}} = 1.33$). For a fixed entrance angle of the light ray inside the diffuser, the exiting ray will be deflected more toward the surface normal ($n_{\mathrm{diffuser}} = 1.5 - 1.6$ at 635 nm), resulting in a more peaked profile.[26] Furthermore, in water, the maximum in the longitudinal radiance profile of the RD40 moves forward, i.e., toward the distal end of the diffuser. As the difference between the refractive indices of the diffuser and the surrounding media drops, the light will exit the diffuser on average after fewer reflections and therefore fewer scattering events, resulting in an increase in radiance at the distal end. However, the azimuthal profile is only little affected and no prominent forward peaking occurs. The overall reduction of the longitudinal radiance when measuring in water is due to specular reflections at the surfaces where the refractive index changes. The transition from water over borosilicate glass ($n_{\mathrm{glass}} = 1.48$) to air leads to a light reduction of ~4%.[35] However, the radiance profiles of the RD40 measured in water are adequate for an interstitial use of the diffuser. The light becomes quickly isotropic after propagating for a few $\mu_s'^{-1}$ in the tissue. In contrary, in the region close to the tissue surface and known as the build-up region, the fluence rate can reach values several times greater than the nonscattered fluence rate,[14] which may lead to issues with the hot spots observed on the longitudinal radiance profile of the RD40 at 808 nm.

The results obtained by this specific goniometer setup demonstrate its usability for the quality control between a few diffuser units. For the analysis of a large number of fibers, other methods may have to be considered if a more rapid means of assessment are required. The setting up of the experiment requires a fair degree of skill, which is nontrivial, and measuring the full three-dimensional radiance distribution is time consuming. This may be all together inconvenient for industrial use; however, this test method is of particular interest when designing or optimizing diffuser parameters. Especially, the knowledge of the angular radiance components and the overall performance of a diffuser in a media other than air are highly important for developing the new diffuser types. Finally, the full description of the three-dimensional radiance distribution is also of great interest when the light propagation in soft tissues is simulated by Monte-Carlo methods.[8,14,28] A radiance distribution measured in water can tremendously simplify the modeling of the light source in such simulations.

5 Conclusions

Light-based treatments of diseases depend, among other aspects, on how and to what extent the light is distributed in biological material. Thus, the knowledge of the characteristics of the light source is crucial. The objective of this study was to develop light detector setup able to measure the three-dimensional radiance distribution of a cylindrical light diffuser in air and liquid.

A CCD-camera-based goniometer setup was developed for the measurement of the radiance of a cylindrical light diffuser. The radiance along the diffuser length and all its angular components was measured by performing a single scan along the azimuthal angle. Then, the three-dimensional radiance distribution was reconstructed by a dedicated data processing algorithm. The spatial resolution was in the submillimeter range, the lowest detectable value of radiance 0.1 $\mathrm{mW\,cm^{-2}\,sr^{-1}}$.

The longitudinal and angular profiles of the RD40 diffuser measured in air and water were very homogeneous at wavelengths of 635, 671, and 808 nm. At 808 nm, relative variations in the profile were maximal, most likely due to the manufacturing process of the diffuser that is optimized for wavelengths in the range of 630 to 690 nm. In water, profiles were less Lambertian than in air. An increased refractive index was found to increase radial light emission due to better index matching. In air and water, no pronounced forward-directed emission was detected, in contrary to what was reported for diffusers from several other independent manufacturers.

Disclosures

G.W. has a financial interest in Medlight SA, which, however, did not support this work. No other conflicts of interest, financial or otherwise, are declared by the authors.

Acknowledgments

The authors thank R. Bays from Medlight SA for the fruitful discussion of the experimental results. We also thank Professor H. van den Bergh for his helpful support in realizing this study. This work was supported in part by the CTI projects 13758.1 and 14660.1, the Swiss National Science Foundation, project CR32I3_159746, and the J. Jacobi grant.

References

1. P. Monnier et al., "Photodetection and photodynamic therapy of 'early' squamous cell carcinomas of the pharynx, oesophagus and tracheobronchial tree," *Laser Med. Sci.* **5**(2), 149–169 (1990).
2. B. F. Overholt et al., "Photodynamic therapy for esophageal cancer using a 180 degree windowed esophageal balloon," *Laser Surg. Med.* **14**(1), 27–33 (1994).
3. B. J. Tromberg et al., "A mathematical model for light dosimetry in photodynamic destruction of human endometrium," *Phys. Med. Biol.* **41**(2), 223–237 (1996).
4. R. Waksman et al., "Intracoronary photodynamic therapy reduces neointimal growth without suppressing re-endothelialisation in a porcine model," *Heart* **92**(8), 1138–1144 (2006).
5. M. D. Altschuler et al., "Optimized interstitial PDT prostate treatment planning with the cimmino feasibility algorithm," *Med. Phys.* **32**(12), 3524–3536 (2005).
6. C. P. Nolsoe et al., "Interstitial hyperthermia of colorectal liver metastases with a us-guided Nd-YAG laser with a diffuser tip: a pilot clinical study," *Radiology* **187**(2), 333–337 (1993).
7. R. Van Hillegersberg et al., "Interstitial Nd:YAG laser coagulation with a cylindrical diffusing fiber tip in experimental liver metastases," *Laser Surg. Med.* **14**(2), 124–138 (1994).
8. A. Pitzschke et al., "Red and NIR light dosimetry in the human deep brain," *Phys. Med. Biol.* **60**(7), 2921–2937 (2015).
9. A. Pitzschke et al., "Optical properties of rabbit brain in the red and near-infrared: changes observed under in vivo, postmortem, frozen, and formalin-fixated conditions," *J. Biomed. Opt.* **20**(2), 025006 (2015).
10. G. Li et al., "Synthesis, comparative photosensitizing efficacy, human serum albumin (site II) binding ability, and intracellular localization characteristics of novel benzobacteriochlorins derived from vic-dihydroxybacteriochlorins," *J. Med. Chem.* **46**(25), 5349–5359 (2003).
11. A. Tremblay et al., "Endobronchial phototoxicity of WST 09 (Tookad), a new fast-acting photosensitizer for photodynamic therapy: preclinical study in the pig," *Photochem. Photobiol.* **78**(2), 124–130 (2003).
12. Z. Huang et al., "Effects of Pd-bacteriopheophorbide (TOOKAD)-mediated photodynamic therapy on canine prostate pretreated with ionizing radiation," *Radiat. Res.* **161**(6), 723–731 (2004).
13. A. Roggan, *Dosimetrie thermischer Laseranwendungen in der Medizin: Untersuchung der optischen Gewebeeigenschaften und physikalisch-mathematische Modellentwicklung*, Fortschritte in der Lasermedizin, Verlagsgruppe Hüthig Jehle Rehm GmbH, Munich, Germany (1997).
14. B. Farina et al., "Monte Carlo simulation of light fluence in tissue in a cylindrical diffusing fibre geometry," *Phys. Med. Biol.* **44**(1), 1–11 (1999).
15. W. M. Star, "Light dosimetry in vivo," *Phys. Med. Biol.* **42**, 763–787 (1997).
16. G. A. Buonaccorsi et al., "Cylindrically distributing optical fiber tip for uniform laser illumination of hollow organs," *Proc. SPIE* **1893**, 214 (1993).
17. J. W. Feather et al., "A method for the construction of disposable cylindrical diffusing fibre optic tips for use in photodynamic therapy," *Laser Med. Sci.* **4**, 229–235 (1989).
18. L. H. P. Murrer, J. P. A. Marijnissen, and W. M. Star, "Ex vivo light dosimetry and Monte Carlo simulations for endobronchial photodynamic therapy," *Phys. Med. Biol.* **40**, 1807–1817 (1995).
19. T. M. Baran, "Cylindrical diffuser axial detection profile is dependent on fiber design," *J. Biomed. Opt.* **20**, 040502 (2015).
20. R. L. Kozodoy et al., "Three-dimensional characterization of the light distribution from diffusing cylindrical optical-fiber tips," *Appl. Opt.* **33**, 6674–6682 (1994).
21. L. M. Vesselov, W. Whittington, and L. Lilge, "Performance evaluation of cylindrical fiber optic light diffusers for biomedical applications," *Laser Surg. Med.* **34**(4), 348–351 (2004).
22. L. Vesselov, W. Whittington, and L. Lilge, "Design and performance of thin cylindrical diffusers created in Ge-doped multimode optical fibers," *Appl. Opt.* **44**, 2754 (2005).
23. L. Lilge, L. Vesselov, and W. Whittington, "Thin cylindrical diffusers in multimode Ge-doped silica fibers," *Laser Surg. Med.* **36**(3), 245–251 (2005).
24. W. Small, IV et al., "Fabrication and characterization of cylindrical light diffusers comprised of shape memory polymer," *J. Biomed. Opt.* **13**(2), 024018 (2008).
25. J. C. Mizeret et al., "New distributors for homogeneous and monitorable light delivery in photodynamic therapy," *Proc. SPIE* **2323**, 58 (1995).
26. L. H. P. Murrer, J. P. A. Marijnissen, and W. M. Star, "Light distribution by linear diffusing sources for photodynamic therapy," *Phys. Med. Biol.* **41**, 951–961 (1996).
27. P. M. Ripley, T. N. Mills, and J. A. S. Brookers, "Measurement of the emission profiles of cylindrical light diffusers using a video technique," *Laser Med. Sci.* **14**(1), 257–268 (1999).
28. Z. Guo, S. R. Daly, and J. K. Matson, "Optical modeling of cylindrical light sources within tissue," *Proc. SPIE* **4961**, 114 (2003).
29. P. M. Ripley et al., "A comparative optical analysis of cylindrical diffuser fibres for laser therapy using fluorescence imaging," *Laser Med. Sci.* **14**(4), 257–268 (1999).
30. R. McCluney, *Introduction to Radiometry and Photometry*, Artech House, Inc., Boston (1994).
31. *Cylindrical Light Diffuser Model RD. Ch. des Larges-Pièces B*, CH-1024 Ecubles, Switzerland (2015).
32. *Frontal Light Distributor Model FD1. Ch. des Larges-Pièces B*, CH-1024 Ecubles, Switzerland (2015).
33. Y. Koike, *Fundamentals of Plastic Optical Fibers*, Wiley Blackwell (2014).
34. R. Bonnett and G. Martinez, "Photobleaching of sensitisers used in photodynamic therapy," *Tetrahedron* **57**(47), 9513–9547 (2001).
35. J. P. A. Marijnissen and W. M. Star, "Calibration of isotropic light dosimetry probes based on scattering bulbs in clear media," *Phys. Med. Biol.* **41**, 1191–1208 (1996).

Biographies for the authors are not available.